

Research paper

A solid-like dual-salt polymer electrolyte for Li-metal batteries capable of stable operation over an extended temperature range



Jing Yu^a, Jiapeng Liu^a, Xidong Lin^a, Ho Mei Law^a, Guodong Zhou^a, Stephen C.T. Kwok^{a,b}, Matthew J. Robson^a, Junxiong Wu^c, Francesco Ciucci^{a,b,d,*}

^a Department of Mechanical and Aerospace Engineering, The Hong Kong University of Science and Technology, Hong Kong, China

^b Guangzhou HKUST Fok Ying Tung Research Institute, China

^c Department of Mechanical Engineering, The Hong Kong Polytechnic University, Hong Kong, China

^d Department of Chemical and Biological Engineering, The Hong Kong University of Science and Technology, Hong Kong, China

ARTICLE INFO

Keywords:

Dual salts
Solid-like polymer electrolyte
Coordinated solvents
Li-metal anode
High/low-temperature performance
High conductivity

ABSTRACT

Solid polymer electrolytes (SPEs) and gel polymer electrolytes (GPEs) show great promise for the realization of commercial, high performance Li-metal batteries (LMBs). However, the interfacial and high-temperature instability of GPEs, and the low room-temperature ionic conductivity of SPEs still limit their practical implementation. This article presents a solid-like dual-salt polymer electrolyte (DSPE), consisting of coordinated solvents and thermally stable Li-salts within a temperature-resistant polymer matrix, as a promising new strategy for addressing these issues. The developed DSPE demonstrates high ionic conductivity of 0.16, 0.73, and 1.93 mS cm⁻¹ at -20, 20, and 100 °C, respectively. Li|DSPE|LiFePO₄ batteries using this DSPE deliver an initial discharge capacity of 151 mAh g⁻¹ at 0.5C, a rate performance of 123 mAh g⁻¹ at 3C, and excellent long-term stability with a retained capacity of 143 mAh g⁻¹ after 500 cycles at 0.5C and 23 °C. Further, the battery shows stable cycling between -10 °C and 80 °C. This impressive electrochemical performance is ascribed to the high Li⁺ conductivity of the membrane, the stabilization of the Al current collector, and the formation of a robust, LiF-rich solid-electrolyte interphase containing conductive Li-B-O-based species.

1. Introduction

Li-metal batteries (LMBs) have received considerable attention because the Li-metal anode (LMA) possesses a high theoretical capacity of 3860 mAh g⁻¹, a low redox potential of -3.04 V vs. the standard hydrogen electrode, and a small gravimetric density of 0.534 g cm⁻³ [1–3]. However, LMAs are still not widely used due to their high reactivity with commercial liquid electrolytes, and large volume changes during charge/discharge [4,5]. The gradual consumption of the commercial liquid electrolytes inevitably leads to low Coulombic efficiency (CE) and fast capacity decay [6]. Furthermore, the uncontrolled growth of Li dendrites in the commercial liquid electrolytes can penetrate separators, leading to short circuit and fire hazards [7–10]. These critical issues are more severe below 0 °C and above 60 °C. Nevertheless, batteries with a wide operating temperature range are needed for many critical applications including electric vehicles and grid-scale energy storage in extreme climates [9]. However, wide-temperature LMBs are rarely reported in the literature due to reduced low-temperature Li⁺ conductivity, and safety concerns due to thermal instability of conventional liquid

electrolytes and rapid side reactions between electrode and electrolyte at high temperature [9,11].

Strategies to improve the stability and safety of LMBs include the protection of LMA [12–14], the modification of interfaces [15–17], and electrolyte optimization [18–22]. Polymer-based electrolytes such as solid polymer electrolytes (SPEs) and gel polymer electrolytes (GPEs) are particularly promising for resolving safety issues caused by leakage of liquid electrolytes [23–29]. In addition, polymer-based electrolytes demonstrate good mechanical performance, and show promise for mass production due to their low material and production cost and easy processability [23,25–27,30]. SPEs generally possess lower Li⁺ conductivity than GPEs, with room temperature ionic conductivity of SPEs in the 10⁻²–10⁻³ mS cm⁻¹ range [31,32]. In contrast, GPEs' ionic conductivity can reach 1 mS cm⁻¹ at room temperature through the incorporation of liquid plasticizers [25]. However, these additives sacrifice GPEs' mechanical strength, thermal stability, and safety [23]. An ideal, LMA-compatible polymer electrolyte with a wide operating temperature range would combine the high ionic conductivity of GPEs with the high mechanical strength and thermal stability of SPEs.

* Corresponding author.

E-mail address: francesco.ciucci@ust.hk (F. Ciucci).

Li salts play a crucial role in determining the capacity and stability of polymer electrolytes [33–35]. Lithium hexafluoride phosphate (LiPF_6) is widely used in commercial applications due to its balance of conductivity and chemical stability [34]. However, its poor thermal stability often leads to a short battery life span and reduced stability above 60 °C [36]. To increase battery operating temperature range, Li salts with high thermal and chemical stability, such as lithium borates (e.g. lithium bis(oxalato)borate (LiBOB)) and lithium imides (e.g. lithium bis(trifluoromethanesulfonyl)imide (LiTFSI)) have been proposed [33]. However, LiTFSI induces the corrosion of the Al current collector, thus reducing the cycle life [37], and LiBOB has a relatively low ionic conductivity in conventional carbonate solvents [38]. Recently, dual-salt electrolytes have been widely employed in liquid electrolytes to increase the conductivity, stabilize the electrode/electrolyte interface, and enhance battery cycle life [33,39–41]. For example, Xiang et al. demonstrated that a 1.0 M dual-salt LiTFSI-LiBOB in ethylene carbonate (EC) and ethyl methyl carbonate (EMC) forms a stable solid electrolyte interphase (SEI) layer, which effectively protects the Al current collector from corrosion [42]. However, this dual-salt electrolyte is formulated with a high volume of organic solvents, which inevitably causes safety problems, especially in the case of overheating or accidents. A highly concentrated electrolytes (e.g. 4.0 M) was reported to stabilize the solvent and anode by generating a high-quality SEI layer on LMA [18]. However, increasing the salt concentration adds to the costs. Little work has been reported on dual-salt electrolytes within a temperature-resistant polymer matrix. This combination is of particular interest as interactions between Li salts, solvents and the polymer matrix may further enhance ionic conductivity [43,44].

This article proposes a dual-salt polymer electrolyte (DSPE) that can enhance LMB capacity, improve cycling stability, and increase the operating temperature range over conventional liquid electrolytes, while mitigating safety challenges. In addition, this DSPE has potential for scalable production. The reported DSPE demonstrates high conductivity of 0.16, 0.73, and 1.93 mS cm⁻¹ at -20, 20, and 100 °C. Furthermore, the Li/LiFePO₄ batteries assembled with this DSPE exhibit high discharge capacities, excellent rate capabilities, and cycling stability at temperatures up to 80 °C and down to -10 °C.

2. Experimental section

2.1. Preparation of polymer electrolytes

The free-standing DSPE membrane was prepared by film casting. First, 0.172 g of LiTFSI (99%, Sigma-Aldrich) and 0.078 g of LiBOB (98%, Dkmchem) were stirred into a mixture of 0.49 mL of propylene carbonate (PC, 99%, Dkmchem), 0.49 mL of EC (99%, Alfa Aesar), and 0.02 mL of fluoroethylene carbonate (FEC, 98%, Alfa Aesar), to obtain a 1.0 M dual-salt solution. The weight ratio of LiTFSI and LiBOB was determined after considering the ionic conductivity and stability of DSPE against the Al current collector, as well as the previous results in literature [40,45]. 0.45 g of polyvinylidene fluoride (PVDF, Kynar HSV900, Arkema) and 4.0 mL of N, N-dimethylformamide (DMF, 99.9%, Prolabo) were then added to the 1.0 M solution, and magnetically stirred at 80 °C for 10 h to form a viscous solution. Finally, the resulting solution was cast onto a glass dish and dried at 100 °C for 2 h in a vacuum oven to obtain a free-standing membrane of DSPE. For comparison, 1.0 M LiTFSI and 1.0 M LiBOB solutions were also prepared respectively to obtain free-standing membranes of LiTFSI polymer electrolyte (LiTFSI-PE), and LiBOB polymer electrolyte (LiBOB-PE). These polymer electrolytes were stored in a glovebox (Super 1220/750, Mikrouna) under ultrapure Ar (99.999%, Air Products).

2.2. Cathode preparation

The cathode slurry was prepared by mixing LiFePO₄ (LFP, Aleees), conductive carbon black (TIMICAL SUPER C65, MTI), and PVDF with

a weight ratio of 8:1:1 in a N-methyl-2-pyrrolidone (NMP, 99.9%, MTI) solvent. After magnetic stirring on a hot plate for 12 h, the slurry was cast onto an Al foil using a doctor blade and dried at 90 °C for 8 h. Finally, the cathode (mass loading 2–3 mg cm⁻²) was punched into disks with a diameter of 12 mm.

2.3. Physical characterizations

Morphology and elemental compositions were measured using scanning electron microscope (SEM, JEOL-6700F and JEOL-7100F) and energy-dispersive X-ray spectroscopy (EDX, JEOL-6700F and JEOL-7100F). Uniaxial tensile testing was performed using a UTM-I2 universal testing machine following the ASTM D412 standard with a crosshead speed of 10 mm min⁻¹. Thermogravimetric analysis (TGA) was carried out using a TA Q5000 (TA Instrument) from room temperature to 550 °C under flowing N₂. X-ray diffraction (XRD) was conducted using a PANalytical Empyrean Pro-diffractometer with Cu K α radiation ($\lambda = 1.5406 \text{ \AA}$) in the 2θ range from 10 to 90°. Fourier-transform infrared (FTIR) spectra were recorded with a Bruker Vertex 70 FTIR spectrometer. Raman spectra were obtained from a confocal Raman microscope (InVia, Renishaw) with a laser wavelength of 514 nm. X-ray photoelectron spectra (XPS) were collected using a PHI5600 X-ray photoelectron spectrometer. Time-of-flight secondary ion mass spectrometry (TOFSIMS) was carried out with TOFSIMS V (ION-TOF GmbH), and the obtained data were analyzed by SurfaceLab 7 Software Package. The Li-metal electrodes from the disassembled cells were first cleaned with dimethyl carbonate (DMC, AR, Dkmchem) three times and then stored in the glovebox before the SEM and XPS measurements.

2.4. Electrochemical characterizations

A Bio-Logic VSP300 electrochemical workstation was employed for recording electrochemical impedance spectra (EIS). EIS were recorded over a frequency range from 7 MHz to 1 Hz with a 10 mV AC signal. To measure Li⁺ conductivity, electrolyte membranes were sandwiched between stainless steel (SS) disks in a SS|polymer electrolyte|SS (CR2032) configuration. The ionic conductivity, σ , was calculated using the equation, $\sigma = l / RA$, where l is the thickness of the electrolyte membrane, R is the resistance measured by EIS, and A is the contact area between the electrolyte membrane and SS. The conductivity can be fitted to the Vogel-Tamman-Fulcher (VTF) equation [46]:

$$\sigma = \sigma_0 \times T^{-0.5} \exp\left(-\frac{E_a}{(T - T_0)k_B}\right) \quad (1)$$

where σ_0 is the pre-exponential factor, k_B is the Boltzmann constant, T_0 is the reference temperature, and E_a is the pseudo-activation energy.

Symmetric Li/Li cells were analyzed by chronoamperometry and EIS to estimate the Li⁺ transference number, t_{Li^+} . t_{Li^+} was computed using:

$$t_{\text{Li}^+} = \frac{I_{ss}(\Delta V - I_0 R_0)}{I_0(\Delta V - I_{ss} R_{ss})} \quad (2)$$

where I_0 and I_{ss} are the initial and steady-state currents from chronoamperometry measurements, with an applied DC potential difference (ΔV) of 10 mV, and R_0 and R_{ss} are the initial and steady state resistances from EIS.

To evaluate the electrochemical stability of the electrolyte membranes, cyclic voltammetry (CV) was used in the Li|DSPE|SS cell at a sweeping rate of 5 mV s⁻¹. To evaluate the stability of Al, linear sweep voltammetry (LSV) was carried out for Li|LiTFSI-PE|Al and Li|DSPE|Al cells from 3.0 to 5.0 V at a scan rate of 0.1 mV s⁻¹. Both CV and LSV were controlled by a Bio-Logic VSP300 electrochemical workstation. Li/Li symmetric cells were assembled for evaluating the Li stripping and plating stability using a battery testing system (CT2001A, LANHE). Galvanostatic charge-discharge curves of Li/LFP batteries were measured within the voltage range from 2.5 to 4.2 V vs. Li/Li⁺ using the

same battery testing system (CT2001A, LANHE). All the temperature-dependent electrochemical measurements were conducted in an isolated chamber (SU-242-5, ESPEC North America). All preparation procedures were performed inside the glovebox (Mikrouna, $[O_2] < 0.1$ ppm, $[H_2O] < 0.1$ ppm) filled with ultrapure Ar ($\geq 99.999\%$, Air products).

2.5. Computation

Ab initio molecular dynamic (MD) simulations were carried out with the CP2K package [47,48] with an energy cutoff of 500 Ry for the auxiliary plane-wave basis set expansion and 60 Ry for the relative energy cutoff. For each element, the valence electrons were modeled with the atom-centered Gaussian double-zeta basis set augmented with a set of *d*-type or *p*-type polarization functions (DZVP-MOLOPT-SRGTH). The core electrons were approximated by the norm-conserving Goedecker-Teter-Hutter (GTH) pseudopotentials [49,50]. The Perdew-Burke-Ernzerhof functional was used for the exchange correlations [51]. For the self-consistent field (SCF) calculations, the orbital transformation (OT) with direct inversion of the iterative subspace (DIIS) energy minimizer was used until the energy converged into 10^{-6} atomic unit [52]. The MD simulations were performed under the isothermal-isobaric (NPT)-isotropic ensemble using a canonical sampling velocity rescaling (CSV) with a 10 fs time constant [53]. The external pressure was set to 1 bar with a barostat time constant of 50 fs. The nuclei trajectories were computed with a time step of 0.5 fs. The MD simulations were carried out at 300 K with a temperature tolerance of 100 K for a total of 5000 steps (2.5 ps). After that, 10 structures with the lowest potential energies in the last 1000 steps were selected for the geometric optimization. The initial structures of Li^+ with different solvent molecules for the MD simulations were generated with the packmol package [54] to create cubic boxes with 3D periodic boundary conditions and initial density of 1 g cm^{-3} . Molar ratios of EC:PC: Li^+ = 7:6:1, 15:0:1, and 0:12:1 were used to simulate the 1 M Li salt in solvent with EC:PC = 0.49 mL:0.49 mL, 0.98 mL:0.0 mL, and 0.0 mL:0.98 mL, respectively. As each system contained only one Li^+ , the total charge and spin multiplicity were set to 1. The initial side length of the computational boxes for the system of EC, PC, and EC + PC mixture were taken to be 13.0 Å, 12.7 Å and 12.7 Å, respectively.

Following MD simulation, a two-step geometric optimization was performed. First, the 10 structures selected from the above MD simulations for each system were optimized with the Vienna *ab initio* simulation package (VASP) [55,56] with a plane-wave basis set defined by a kinetic energy cut-off of 400 eV. Second, the structure with the minimum energy for each system was regarded as the initial configuration for further optimization in Gaussian 09 D.01 with the B3LYP functional [57,58]. VASP geometric optimization utilized the projector augmented wave (PAW) [59] pseudopotentials with valence-electron configurations of $1s^1$, $1s^22s^1$, $2s^22p^2$, and $2s^22p^4$ for H, Li, C, and O, respectively. The electron exchange-correlation was described using the Perdew-Burk-Ernzerhof (PBE) functional [51]. To simulate the system with one Li^+ , one electron was removed from each system to make the system charging 1 |e|. Both the lattice parameters and the ionic positions were allowed to relax until the total energy converged to 10^{-5} eV. For the calculations in Gaussian, the 6-31++G(d, p) basis set was used for Li, C, O, and H atoms. To maintain consistency with the MD simulations, the total charge was set to 1 |e| and the spin multiplicity was also set to 1. To simplify the computations, only the solvent molecules that coordinate with the Li^+ in a cut-off of 2.6 Å were modeled in the second step geometric optimization. For EC or PC solvent, the Li^+ was coordinated with 4 O atoms either from EC or PC. For the mixed EC and PC solvent, the Li^+ was coordinated with 4 O atoms from EC and 1 O atom from PC. Therefore, systems with a molar ratio of EC:PC: Li^+ = 4:0:1, 0:4:1, and 4:1:1 were chosen to simulate the Li^+ in EC, PC, and the mixed EC and PC solvents, respectively. After the geometric optimization in Gaussian, the coordination environment for Li^+ with EC and PC remains unchanged, whereas the Li^+ coordinates with 3 O atoms from EC and 1 O atom from

PC for the mixed solvent. All the optimized structures were confirmed as stable with no imaginary vibrational frequencies. The Brillouin zone was sampled only with Γ point for all the calculations.

The interaction between the Li^+ and solvent molecules was calculated by the binding energy as $\Delta E_b = E_{\text{complex}} - E_{\text{solvent}} - E_{Li^+}$, where the E_{complex} is the energy of the solvent molecules and a single Li^+ system, E_{solvent} is the energy of the solvent molecules optimized at the same level, and E_{Li^+} is the energy of one Li atom with a charge of 1. Zero-point energy (ZPE) corrections were also included in the ΔE_b . Similarly, the enthalpy and free energy of solvation (ΔH_{sol} and ΔG_{sol}) at 298.15 K were also calculated following the same procedure, $\Delta H_{sol} = H_{\text{complex}} - H_{\text{solvent}} - E_{Li^+}$, and $\Delta G_{sol} = G_{\text{complex}} - G_{\text{solvent}} - E_{Li^+}$ [60].

All density functional theory (DFT) calculations were performed with Gaussian 09. The 6-31++G (d,p) basic set together with a hybrid B3LYP functional [57] were employed in all the computations. First, the structures of all molecules were optimized, and the structures were then used to calculate the energy of the molecular orbitals.

3. Results and discussion

3.1. Physical and chemical properties

This DSPE combines the advantages of SPEs and GPEs; its relative performance in comparison to general GPEs and SPEs is schematically illustrated in Fig. 1a. The DSPE membrane was prepared by solution casting followed by solvent evaporation, as shown in Fig. 1b. In addition to introducing dual salts in PVDF, commonly applied organic liquid solvents with high dielectric constant such as cyclic EC and PC were included to increase the DSPE membrane's ionic conductivity [61]. PC was adopted due to its low cost, and high-boiling and low-freezing temperatures [62]. FEC was added since it can enhance film formation and effectively suppress side reactions by generating a LiF-rich protective layer, thereby improving the electrochemical stability [24, 63]. Details regarding the preparation method can be found in the experimental section. The as-produced DSPE has an interconnected microstructure (Fig. 1c) with a thickness of 100 μm (Fig. 1d) and is flexible and bendable (Fig. 1e). EDX analysis of DSPE (Fig. S1) suggests a uniform distribution of PVDF, LiTFSI, and LiBOB. In addition, the DSPE membrane exhibits a tensile strength of 12.4 MPa and Young's modulus of 23.3 MPa, a value significantly higher than that of GPEs (Fig. S2) [25]. Moreover, the DSPE membrane shows a strain to failure of $\sim 261.8\%$ (Fig. 1f).

TGA was used to characterize the DSPE's thermal stability. As shown in Fig. 1g, the membrane shows no weight loss up to 90 °C and <20 wt.% loss up to 290 °C. This weight loss is less than SPE with plastic crystal glutaronitrile (35 wt.% at 200 °C) [64]. Furthermore, the low weight loss demonstrates that the DSPE's liquid content is significantly lower than that of the reported PVDF-based GPEs (~ 50 wt.%) [44], and therefore it suggests a significant liquid loss during drying. However, a limited amount of residual DMF, EC, and PC is likely present in the DSPE membrane after drying at 100 °C for 2 h in a vacuum oven. Raman spectra show a shift from 658 to 673 cm^{-1} , suggesting that residual DMF is trapped within the DSPE membrane and forms $[Li(DMF)_x]^+$, which may be beneficial for the cell performance [44]. Peaks corresponding to free EC and PC are not observed in the Raman spectra (Fig. S3), indicative of bound solvents in the DSPE membrane. Weight loss in the 290–350 °C range corresponds to the decomposition of LiBOB and LiTFSI [35]. TGA results also demonstrate a low weight percentage of Li salts (27.7 wt.%) relative to a highly concentrated dual-salt electrolyte (52.3 wt.%) [18]. Low content of Li salts may contribute to reducing costs. We schematically illustrate the weight percentage of each component in Fig. S4 and list the key parameters in Table S1. In sharp contrast, a commercial liquid electrolyte containing 1.0 M $LiPF_6$ in EC/DMC/EMC is unstable at a slightly elevated temperature, e.g., a weight loss of $\sim 40\%$ can be observed when the temperature increases from 23 °C to 58 °C (Fig. S5). In

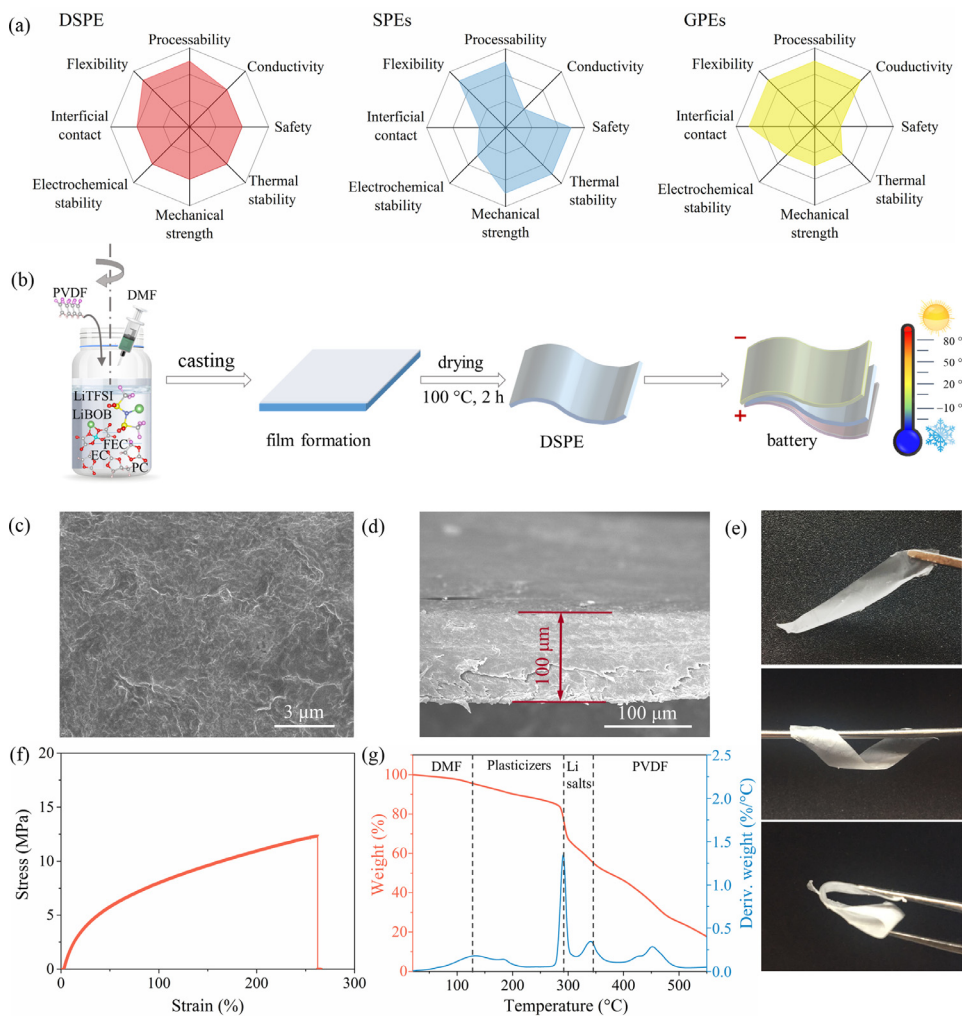


Fig. 1. (a) Radar maps of the strengths of the DSPE membrane in comparison to SPEs and GPEs. (b) A schematic diagram of the preparation of the DSPE membrane. (c) Top-view and (d) cross-sectional SEM images of the DSPE membrane. (e) Optical photos of the free-standing, flexible and bendable DSPE membrane. (f) Stress-strain and (g) TG curves of the DSPE membrane.

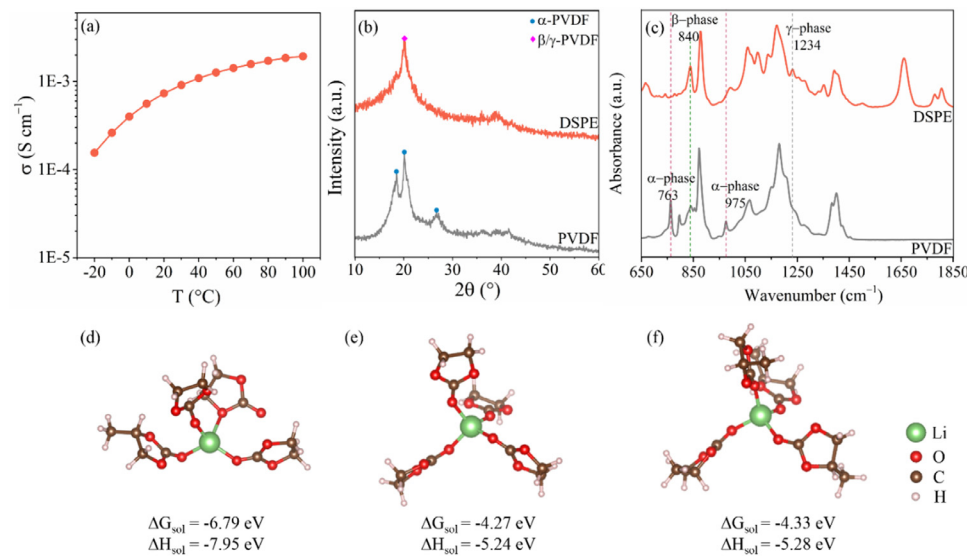


Fig. 2. (a) Temperature-dependent conductivity of the DSPE membrane. (b) XRD patterns and (c) FTIR spectra of DSPE and PVDF. Optimized structures for Li⁺ with different solvent molecules: (d) EC:PC; (e) EC; and (f) PC.

short, this novel flexible and bendable solid-like DSPE not only possesses good mechanical properties but also exhibits high thermal stability.

3.2. Ionic conductivity and Li⁺ transference number

Batteries need electrolytes with high ionic conductivity to facilitate fast charge/discharge rates required in high power applications. The

ionic conductivity of DSPE derived from the Nyquist plots measured between -20 and 100 °C (Fig. S6) are shown in Fig. 2a. The ionic conductivity of DSPE is as high as 0.73 mS cm⁻¹ at 20 °C, significantly higher than that of common SPEs (Fig. S2). In addition, the DSPE membrane achieves 0.16 mS cm⁻¹ at -20 °C, and reaches 1.93 mS cm⁻¹ at 100 °C. It is worth noting that the nonlinear ionic conductivity-temperature relation ($\ln(\sigma T)$ vs. $1/T$) suggests that conduction involves ionic hop-

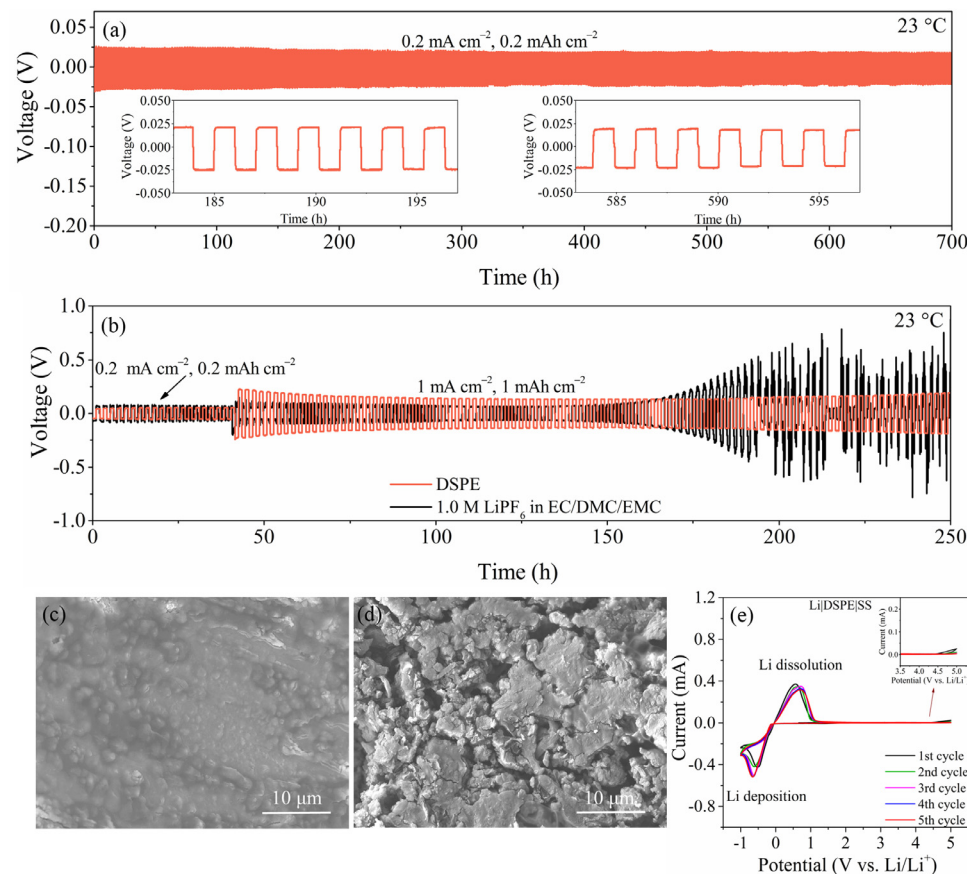


Fig. 3. Plating and stripping behavior of (a) the symmetric Li|DSPE|Li cell at 0.2 mA cm⁻² and 0.2 mAh cm⁻², and (b) the symmetric Li|DSPE|Li and Li|liquid electrolyte|Li cells. Top-view SEM images of the LMA after cycling in the (c) Li|DSPE|Li and (d) Li|liquid electrolyte|Li cells. (e) Cyclic voltammogram of the Li|DSPE|SS cell.

ping motion coupled with relaxation/breathing and segmental motion of polymeric chains [23,65,66]. Therefore, the identified ionic conduction mechanism of DSPE in this work differs from that of GPEs. In GPEs, the solvated Li-ions play a dominant role in determining conductivity, while the polymer chains rarely take part in the transportation of Li⁺ [44]. The activation energy (E_a) of the DSPE membrane, which is finally calculated using the VTF empirical relation [46,64], is 0.039 eV, is lower than that of general SPEs, indicating a fast Li⁺ migration (Fig. S7).

In addition to the general contribution of Li salts, the relatively high ionic conductivity of DSPE could be ascribed to the phase transition of PVDF. The phases of PVDF are dependent on the molecular chain conformation, which is strongly influenced by fabrication processes (e.g. mechanical and thermal), and polymer composition [67]. As shown in Fig. 2b, the pristine PVDF powder is in its α -phase with characteristic XRD peaks at 18.2°, 20.0°, and 26.4°. Meanwhile, the most prominent peak of DSPE occurs at 20.1° and the intensity of the other two peaks decreases significantly, indicating a phase transition from the nonpolar α to the polar β/γ phase(s) [68,69]. FTIR spectra (Fig. 2c) further confirm the α to β/γ phase transition by the disappearance of 763 cm⁻¹ and 975 cm⁻¹ bands (α -phase) [70], and the appearance of the 840 cm⁻¹ and 1234 cm⁻¹ phases [70,71].

Ideal electrolytes possess high Li salt solubility in non-aqueous solvents. To investigate the solubility of EC, PC, and the combination of EC and PC with Li⁺, *ab initio* simulations were used to calculate the enthalpy of solvation and the Gibbs free energy. As shown in Table S2, the enthalpy of solvation, ΔH_{sol} , for these three different systems is negative, implying that all these complexes can dissolve Li salts and the formation of Li-carbonate is thermodynamically favorable. The ΔH_{sol} for the EC and PC mixture has the lowest value, implying that the combination of EC and PC has higher solubility for Li salts compared to EC and PC alone. The free energies, ΔG_{sol} , computed for all three dif-

ferent systems are also negative, suggesting that the solvation process is exothermic and spontaneous. Among the investigated solvents, the binary mixture of EC and PC has the lowest free energy of solvation (Fig. 2d-f and Table S2) [60]. Therefore, the combination of EC and PC as solvents effectively solvates Li salts, enhancing the ionic conductivity of DSPE.

Li⁺ transference number, t_{Li^+} , is a critical factor for Li⁺ transportation in polymer electrolytes [72]. From the EIS and direct current polarization curves in Fig. S8a, the t_{Li^+} of DSPE is 0.56, a value higher than that of typical GPEs and SPEs ($t_{Li^+} < 0.5$) [25,72], and much higher than that of the commercial 1.0 M LiPF₆ in EC:DMC:EMC (1:1:1, vol.%) ($t_{Li^+} = 0.24$, Fig. S8b). The low Li⁺ transference number of liquid electrolytes is due to the preferential solvation of Li⁺ over its counterion, resulting in a bulky solvation shell around Li⁺ [72]. Conversely, the residual solvents in DSPE are limited, which may lead to a greatly shunk solvation shell around Li⁺, thus enhancing the Li⁺ transference number. Furthermore, PVDF in DSPE acts as more than just a solid matrix for the solvents and salts, as the polymeric chains may influence the short-range Li⁺ mobility and thus transference number [73]. Moreover, the size of salt anions (e.g. TFSI⁻) in DSPE is relatively large compared to that of PF₆⁻.

3.3. Compatibility with electrodes and battery performance

To assess the compatibility of DSPE with Li metal, a Li/Cu cell with DSPE and a Li/Cu cell with 1.0 M LiPF₆ in EC:DMC:EMC (1:1:1, vol.%) liquid electrolyte were compared (Fig. S9). The first cycle CE reaches ~78% in the Li|DSPE|Cu cell, increasing to ~93% and remaining stable over 100 cycles. In contrast, the Li|liquid electrolyte|Cu cell shows a relatively low average CE of ~82%, decreasing to 70% after 100 cycles. The initial results indicate that the Li/DSPE interface is more stable than that of the Li/liquid electrolyte. Furthermore, Li stripping/plating

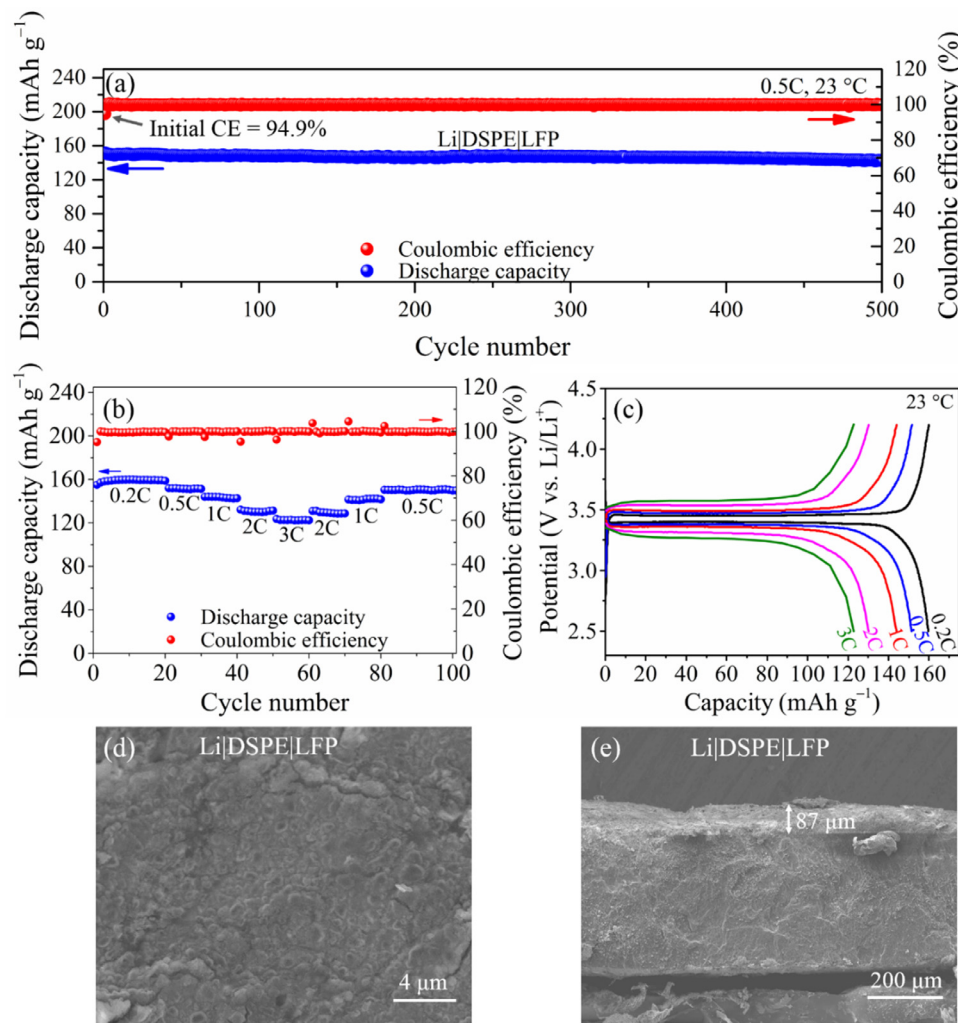


Fig. 4. (a) Cycling performance of the Li|DSPE|LFP cell at 0.5C at 23 °C. (b) Rate performance of the Li|DSPE|LFP cell at 23 °C. (c) Typical charge/discharge curves of the Li|DSPE|LFP cell at different C-rates. (d) Top-view and (e) cross-sectional SEM images of the Li-metal electrode of the Li|DSPE|LFP cell after cycling.

measurements were conducted using a symmetric cell configuration. Remarkably, the Li|DSPE|Li cell has a stable voltage response over 700 h with a capacity of 0.2 mAh cm⁻² at a current density of 0.2 mA cm⁻² (Fig. 3a). Moreover, the Li|DSPE|Li cell is stable in cycling for more than 250 h with a current density of 1.0 mA cm⁻² and a capacity of 1.0 mAh cm⁻². In contrast, as shown in Fig. 3b, when the current density increases to 1.0 mA cm⁻², the voltage of the symmetric cell containing the liquid electrolyte with 1.0 M LiPF₆ in EC:DMC:EMC (1:1:1, vol.%) and Celgard 2400 membrane as the separator greatly increases after 150 h, and the cell short-circuits after 196 h. The excellent stability of the DSPE membrane is likely due to the formation of a uniform, dense, and stable interface between LMA and DSPE, as revealed by the SEM image of LMA after cycling (Fig. 3c). However, when the liquid electrolyte is used, the SEM image presents cracks and loose Li on the surface of LMA (Fig. 3d).

To determine the electrochemical window of DSPE, CV of Li|DSPE|SS was performed from -1.0 to 5.0 V at a scan rate of 1 mV s⁻¹. No oxidation current is observed when the voltage exceeds 4.5 V vs. Li/Li⁺ (Fig. 3e). Although the oxidation and reduction peaks do not overlap in the initial cycles due to the gradual formation of SEI, they overlap from the third cycle onwards, indicating reversible Li stripping/plating after forming a stable SEI layer.

To further evaluate the electrochemical performance, Li|DSPE|LFP batteries were assembled. At 23 °C and at a current density of 0.5C, the Li|DSPE|LFP battery, which is operated between 2.5 and 4.2 V, has an initial CE of 94.9% and an initial specific discharge capacity of 151 mAh

g⁻¹ (Fig. 4a). The battery maintains an average CE of 99.9% in subsequent cycles and a discharge capacity of 143 mAh g⁻¹ with a capacity retention of 94.7% after 500 galvanostatic charge/discharge cycles (Fig. 4a). The battery also demonstrates outstanding rate performance, i.e., a discharge capacity of 160 mAh g⁻¹ at 0.2C, 151 mAh g⁻¹ at 0.5C, 144 mAh g⁻¹ at 1C, 130 mAh g⁻¹ at 2C, and 123 mAh g⁻¹ at 3C (Fig. 4b, c). When the current density is subsequently returned to 0.5C, the 151 mAh g⁻¹ capacity is recovered with limited capacity loss over 100 cycles. The Li|DSPE|LFP battery has better CE, cycling stability, and rate performance, compared to single-salt Li|LiTFSI-PE|LFP and Li|LiBOB-PE|LFP batteries (Fig. S10).

The enhanced stability could be related to the suppression of Al dissolution by the introduction of LiBOB to the DSPE membrane [40]. LSV of Li|LiTFSI-PE|Al (Fig. S11a) shows current generation at 4.4 V, whereas the LSV curve of Li|DSPE|Al exhibits no current response up to 5.0 V. Furthermore, after 100 LSV cycles, clear cracks are observed on the Al surface of the Li|LiTFSI-PE|Al cell (Fig. S11b), while no visible cracks are observed for the Li|DSPE|Al cell (Fig. S11c). The suppression of Al corrosion in the Li|DSPE|Al cell is further supported by EDX (Fig. S11d, e), from which a limited Al signal is observed for DSPE, while an evident Al signal is detected for LiTFSI-PE.

The critical role of LiBOB in DSPE not only suppresses the Al corrosion but also guides the formation of a uniform and stable SEI layer, which contributes to enhanced CE and cycling stability [40, 61]. As shown in Fig. S12a, b, the thickness of the SEI layer on the Li-electrode surface of the Li|LiTFSI-PE|LFP cell is ~162 μm. Further, the SEI layer is

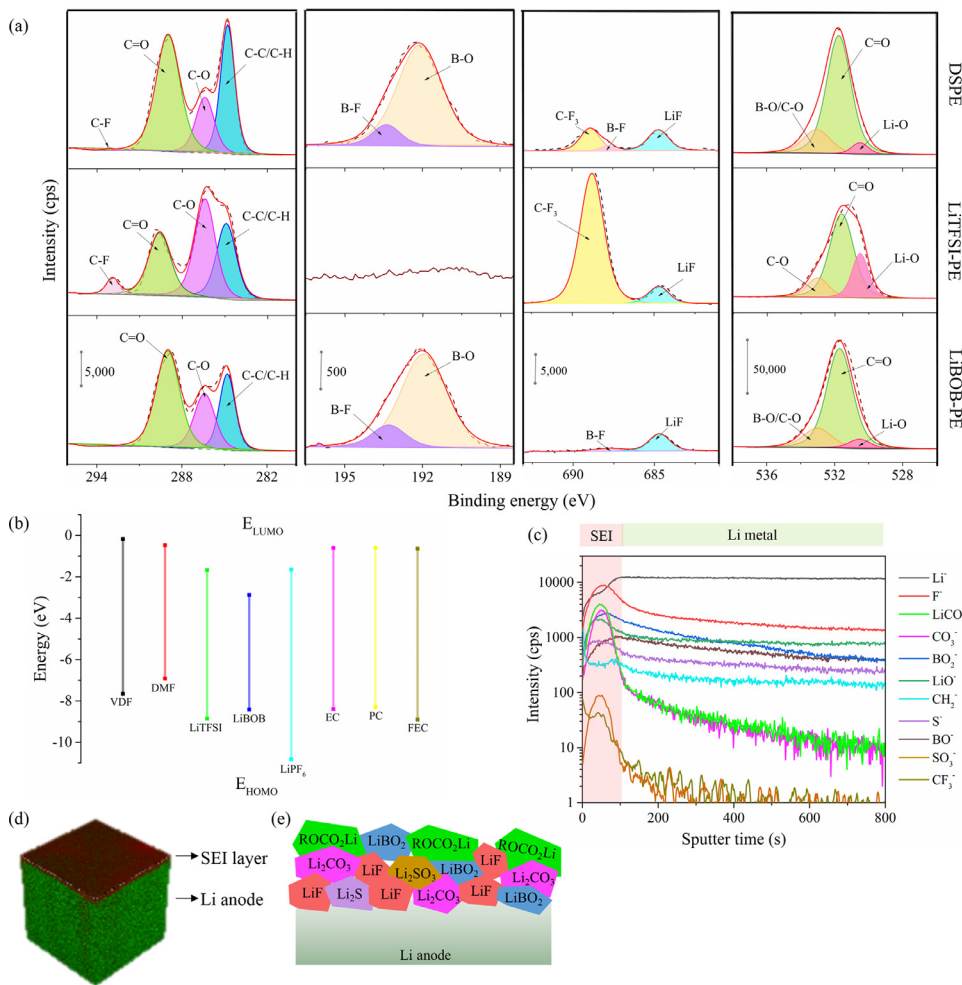


Fig. 5. (a) XPS of the SEI layers from the cycled (200 cycles) LMAs of the Li|DSPE|LFP, Li|LiTFSI-PE|LFP, and Li|LiBOB-PE|LFP cells. (b) Highest occupied molecular orbital (HOMO) and lowest unoccupied molecular orbital (LUMO) energies of the polymer (VDF), lithium salts (LiTFSI and LiBOB) and solvents (DMF, EC, PC, and FEC). (c) TOF-SIMS depth profiles of the LMA of Li|DSPE|LFP after 20 cycles. (d) 3D distribution of the SEI layer on the cycled LMA. (e) A schematic to show the main chemicals formed on the surface of cycled LMA.

covered with mossy Li, implying lack of compactness and overall poor quality. In contrast, both the Li|DSPE|LFP and Li|LiBOB-PE|LFP cells form a uniform and stable SEI after cycling, characterized by the relatively dense and thin Li-electrode surfaces (i.e. $\sim 87 \mu\text{m}$ and $\sim 95 \mu\text{m}$) (Fig. 4d, e & Fig. S12c, d). These results indicate that the addition of LiBOB prevents the formation of mossy dendrites on the Li-electrode surface and thus the formed SEI layer contributes to improved cycling stability [42].

To further understand the superior cycling stability of the battery with DSPE, and to determine the composition of the SEI formed at the interface between Li and DSPE, XPS is obtained on the as-cycled LMA. As shown in Fig. 5a, the C 1 s XPS spectra of SEI layers after cycling LMA with DSPE and LiBOB-PE are similar. The main C 1 s which peaks at 284.8, 286.4, and 289 eV can be assigned to the C—C/C—H, C—O—C, and C=O bonds [18]. The C=O species (e.g. ROCO₂Li, and Li₂CO₃) are dominant in the SEI layer after cycling LMA with DSPE, and their amount is higher than that of the SEI layer with LiTFSI-PE. In addition, greatly decreased C-F peak intensity can be observed after cycling LMA with DSPE compared to that of LMA with LiTFSI-PE, suggesting the reduction of LiTFSI from DSPE is dramatically inhibited due to the prior reduction of BOB⁻ anions [38, 74]. Further, B-O (192.2 eV) and B-F/Li-B-O (193.4 eV) species in B 1 s can be detected in both cycled LMAs of DSPE and LiBOB-PE, confirming that LiBOB participates in the formation of SEI [61]. It has been reported that inorganic Li-B-O species originating from the reduction of LiBOB promote the electrochemical and chemical stability of the SEI layer, thus improving cycling stability [61, 75].

The appearance of LiF (684.7 eV) in the F 1 s spectra (Fig. 5a) suggests the decomposition of FEC and/or LiTFSI. After cycling LMA with LiBOB-PE, LiF formation (684.7 eV) at the SEI is due to FEC decomposition. However, both FEC and LiTFSI are believed to contribute to the creation of LiF in the DSPE and LiTFSI-PE cells. As widely recognized, the generated LiF can function as an effective component in the SEI layer, which contributes to the passivation of Li and the inhibition of dendrite growth [13, 63, 74]. Moreover, the decreased C-F₃ (689.0 eV) peak intensity of the DSPE cell against the LiTFSI-PE cell suggests that LiBOB inhibits the decomposition of LiTFSI, thereby maintaining the high conductivity of the electrolyte. The O 1 s spectra show reduced lithium oxide intensity (530.5 eV) in the SEI layer with DSPE and LiBOB-PE, compared to the SEI layer with LiTFSI-PE. This suggests lithium oxide formation from the reaction between LiTFSI and Li. Moreover, the density functional theory calculation also suggests that LiBOB tends to be preferentially reduced according to the lowest LUMO energy among the investigated solvents and salts (Fig. 5b).

To further analyze the composition of the SEI layer, TOF-SIMS was performed (Fig. 5c). The intensity of detected Li⁺ gradually increases with the sputtering time and tends to stabilize after ~ 100 s, demonstrating the formation of an SEI layer on the cycled LMA. Within the SEI layer, a series of compounds of interest can be detected: (i) F⁻ for LiF; (ii) LiO⁺/LiCO₃⁻/CO₃²⁻ for Li oxides/carbonates/organic carbonates; (iii) BO₂⁻/BO⁺ from LiBOB; (iv) CH₂⁻ for the organic species; and (v) S²⁻/SO₃²⁻/CF₃⁻ from LiTFSI. The high intensities of F⁻, BO₂⁻/BO⁺, and LiCO₃⁻/CO₃²⁻ suggest that LiF, Li-B-O species, and carbonates/organic carbonates are dominant in SEI composition, in line with the XPS re-

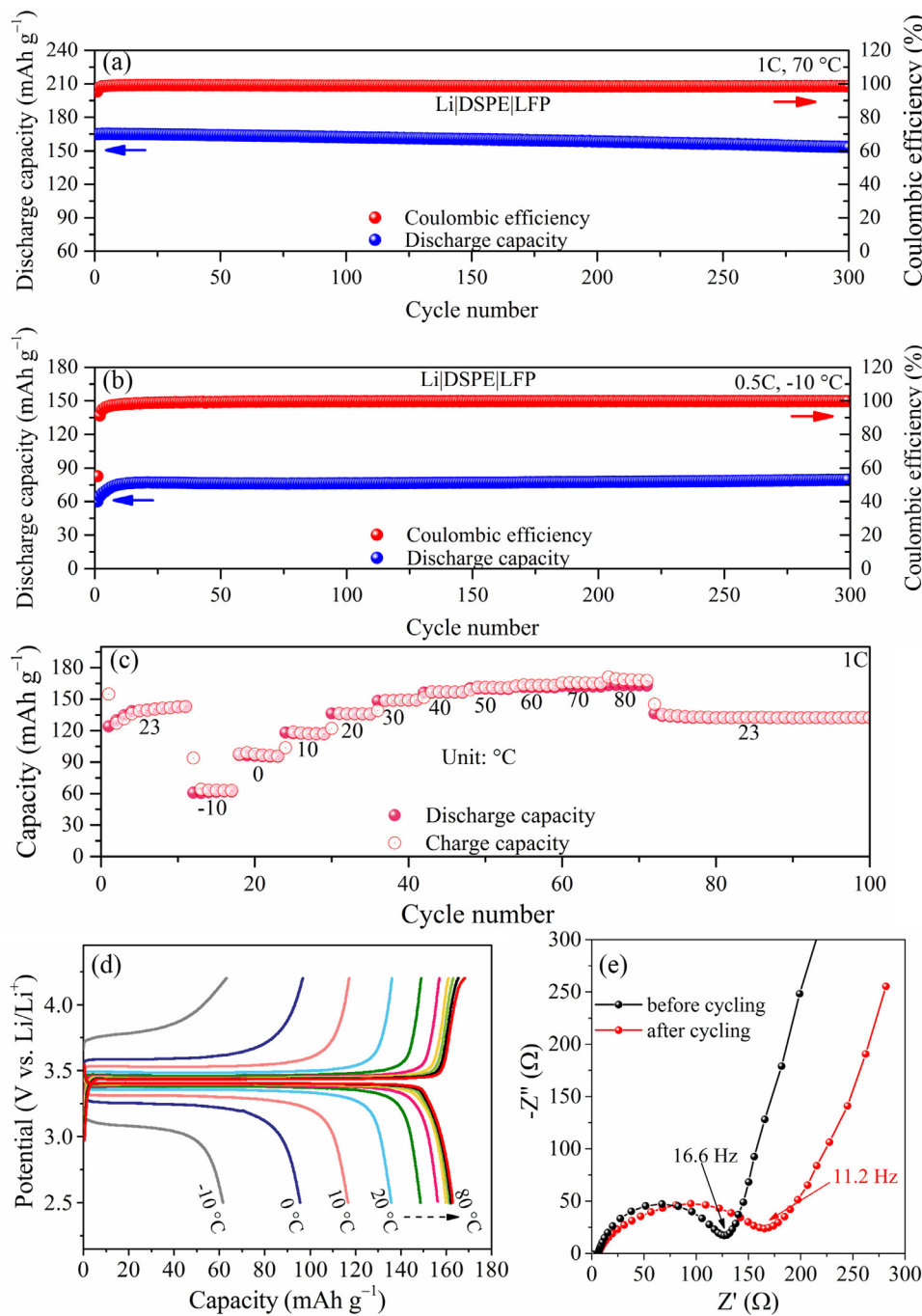


Fig. 6. Cycling performance of the Li|DSPE|LFP cell (a) at 1C at 70 °C and (b) at 0.5C at -10 °C. (c) Cycling performance of the Li|DSPE|LFP cell at a wide temperature range (from -10 to 80 °C) at 1C. (d) Typical charge/discharge curves of the Li|DSPE|LFP cell at different operating temperatures. (e) EIS of the Li|DSPE|LFP cell evaluated between -10 and 80 °C before and after cycling (recorded at 23 °C).

sults. Other organic species (CH_2^-) appear on the top surface of the SEI, indicating that the polymer has minimal influence on SEI formation. The relatively low intensity of the $\text{S}^-/\text{SO}_3^-/\text{CF}_3^-$ signals verify that LiTFSI decomposition is inhibited in the DSPE. The corresponding 3D spatial distribution of the SEI layer on the cycled LMA is shown in Fig. 5d. Following the analysis of the XPS and TOF-SIMS data, the main compositions in the SEI are reported in Fig. 5e.

To demonstrate the feasibility of the DSPE membrane over a wide temperature range, the high- and low-temperature performance of the Li|DSPE|LFP batteries were further investigated. At 70 °C, the Li|DSPE|LFP battery exhibits an initial specific discharge capacity of 165 mAh g⁻¹ and a high CE of 95.5% at 1C (Fig. 6a). The battery is subsequently cycled 300 times, with a capacity retention of 92.9%, i.e., a specific discharge capacity of 153.3 mAh g⁻¹ after 300 cycles. The corre-

sponding voltage plateaus from charge-discharge curves suggest negligible polarization (Fig. S13a) with the total resistance of the Li|DSPE|LFP battery showing a slight increase after cycling (Fig. S13b). The slight increase in resistance indicates that the formed interphase between Li and DSPE facilitates charge transfer [75], likely because of the formation of inorganic LiF and Li-B-O species from the reduction of FEC, LiTFSI, and LiBOB. By comparison, the Li/LFP battery with the commercial liquid electrolyte (1.0 M LiPF₆ in EC: DMC:EMC (1:1:1, vol. %)) fails to operate at 70 °C (Fig. S13c, d). This failure is attributed to electrolyte decomposition and is reflected in the greatly increased resistance from 165 to 528 Ω after 14 cycles (Fig. S13e). Moreover, SEM image of the LMA from the DSPE cell following 300 cycles at 70 °C, demonstrates a visually smooth surface (Fig. S13f). In contrast, the liquid electrolyte cell shows severe Li dendrite growth after 14 cycles at 70 °C (Fig. S13g).

Low-temperature measurements of the Li|DSPE|LFP battery have a retained discharge capacity of 79 mAh g^{-1} after 300 cycles at -10°C at 0.5C (Fig. 6b). Furthermore, the cycling performance of the Li|DSPE|LFP battery is continuously evaluated between -10 and 80°C at 1C, and the outstanding cycling stability is recorded (Fig. 6c). The 1C cycles at -10 , 0, 10, 20, 30, 40, 50, 60, 70, and 80°C lead to specific discharge capacities of 62, 96, 117, 136, 149, 156, 160, 161, 162, and 163 mAh g^{-1} , respectively (Fig. 6d). When the temperature returns to 23°C , the Li|DSPE|LFP battery retains a specific discharge capacity of 131 mAh g^{-1} . The corresponding resistance increases slightly from 127 to 165Ω (Fig. 6e).

The excellent extended temperature operation of the developed DSPE can be ascribed to several factors. At high temperatures, the relatively stable operation of the as-prepared LMBs is due to the presence of thermally stable LiTFSI and LiBOB salts within a temperature-resistant polymer (PVDF) matrix. Moreover, along with the effective passivation and protection of the Al current collector, the addition of LiBOB salt leads to the formation of a uniform and stable SEI layer, as shown in Fig. S13f. Furthermore, high-boiling point (b.p.) solvents (i.e. PC, b.p. 242°C , and DMF, b.p. 153°C), instead of conventionally used solvents (i.e. DMC, b.p. 90°C , and EMC, b.p. 108°C), were used for the preparation of the DSPE membrane, ensuring high stability at high operating temperatures. At low temperatures, the increased stability and capacity originate from the high Li^+ conductivity of the DSPE membrane.

Finally, pouch cells with DSPE were prepared and evaluated. The Li|DSPE|LFP pouch cell delivers an initial discharge capacity of 149 mAh g^{-1} (0.35 mAh cm^{-2}) at 0.5C with an initial CE of 98.9%, and a discharge capacity of 147 mAh g^{-1} after 50 cycles (Fig. S14a). The nail penetration (Video S1) and corner-cutting (Video S2) tests on the pouch cell demonstrate their improved safety over conventional liquid electrolyte Li-ion batteries. There is no detectable smoke or electrolyte leakage after penetration. The pouch cell can consistently power an LED even after bending, corner-cutting, and nail penetration test (Fig. S14b-e), further indicating the improved safety behavior.

4. Conclusion

We have developed a solid-like DSPE for LMBs capable of stable operation over an extended temperature range. The resulting DSPE combines the thermal stability/safety of SPEs and high ionic conductivity of GPEs, reaching ionic conductivity of 0.16, 0.73, and 1.93 mS cm^{-1} at -20 , 20, and 100°C , respectively. This DSPE enables the Li/LFP battery to achieve a high initial discharge capacity of 151 mAh g^{-1} at 0.5C, a high rate performance of 123 mAh g^{-1} at 3C, and excellent long-term stability with a retained capacity of 143 mAh g^{-1} after 500 cycles at 0.5C at 23°C . This battery simultaneously demonstrates an extremely stable cycling performance over a wide operating temperature range (between -10°C and 80°C). These excellent results can be mainly attributed to the proper formulation of the dual salts with mixed solvents in the polymer matrix, the consequent formation of a stable LiF-rich SEI layer containing conductive Li-B-O-based species, and the stabilization of the Al current collector. This work consequently offers a new strategy for the development of practical LMBs.

Declaration of Competing Interest

The authors declare that they have no known competing financial interests or personal relationships that could have appeared to influence the work reported in this paper.

Data for reference

Data will be made available on request.

CRediT authorship contribution statement

Jing Yu: Conceptualization, Methodology, Formal analysis, Investigation, Writing – original draft. **Jiapeng Liu:** Investigation, Software. **Xidong Lin:** Conceptualization, Formal analysis. **Ho Mei Law:** Methodology. **Guodong Zhou:** Methodology. **Stephen C.T. Kwok:** Methodology. **Matthew J. Robson:** Writing – review & editing. **Junxiong Wu:** Writing – review & editing. **Francesco Ciucci:** Resources, Writing – review & editing, Supervision.

Acknowledgement

The authors acknowledge the support from the Research Grants Council of Hong Kong (16227016 and 16204517), the Hong Kong Innovation and Technology Fund (ITS/292/18PP), and the Guangzhou Science and Technology Program (No. 201807010074). The authors thank Prof. Lu-Tao Weng for helping with the TOF-SIMS characterization. The authors are also grateful for the technical assistance from the Materials Characterization and Preparation Facilities (MCPF) of HKUST.

Supplementary materials

Supplementary material associated with this article can be found, in the online version, at doi:10.1016/j.ensm.2021.02.045.

References

- [1] X.-B. Cheng, R. Zhang, C.-Z. Zhao, Q. Zhang, Toward safe lithium metal anode in rechargeable batteries: a review, *Chem. Rev.* 117 (2017) 10403–10473.
- [2] Y. Zhang, T.-T. Zuo, J. Popovic, K. Lim, Y.-X. Yin, J. Maier, Y.-G. Guo, Towards better Li metal anodes: challenges and strategies, *Mater. Today* 33 (2020) 56–74.
- [3] C. Gong, S.D. Pu, X. Gao, S. Yang, J. Liu, Z. Ning, G.J. Rees, I. Capone, L. Pi, B. Liu, G.O. Hartley, J. Fawdon, J. Luo, M. Pasta, C.R.M. Grovenor, P.G. Bruce, A.W. Robertson, Revealing the role of fluoride-rich battery electrode interphases by operando transmission electron microscopy, *Adv. Energy Mater.* (2021) 2003118 n/a.
- [4] N. Wu, P.-H. Chien, Y. Qian, Y. Li, H. Xu, N.S. Grundish, B. Xu, H. Jin, Y.-Y. Hu, G. Yu, J.B. Goodenough, Enhanced surface interactions enable fast Li^+ conduction in oxide/polymer composite electrolyte, *Angew. Chem. Int. Ed.* 59 (2020) 4131–4137.
- [5] L. Alex, C. Matthew, G. Matthe, d. Jack, E. Ahmed, R.D. Jeff, Optimizing cycling conditions for anode-free lithium metal cells, *J. Electrochem. Soc.* 168 (2021) 020515.
- [6] D. Aurbach, E. Zinigrad, Y. Cohen, H. Teller, A short review of failure mechanisms of lithium metal and lithiated graphite anodes in liquid electrolyte solutions, *Solid State Ionics* 148 (2002) 405–416.
- [7] D. Lin, Y. Liu, Y. Cui, Reviving the lithium metal anode for high-energy batteries, *Nat. Nanotechnol.* 12 (2017) 194–206.
- [8] Z. Geng, J. Lu, Q. Li, J. Qiu, Y. Wang, J. Peng, J. Huang, W. Li, X. Yu, H. Li, Lithium metal batteries capable of stable operation at elevated temperature, *Energy Storage Mater.* 23 (2019) 646–652.
- [9] X. Shangguan, G. Xu, Z. Cui, Q. Wang, X. Du, K. Chen, S. Huang, G. Jia, F. Li, X. Wang, D. Lu, S. Dong, G. Cui, Additive-assisted novel dual-salt electrolyte addresses wide temperature operation of lithium–metal batteries, *Small* 15 (2019) 1900269.
- [10] X. Lin, G. Zhou, J. Liu, J. Yu, M.B. Effat, J. Wu, F. Ciucci, Rechargeable battery electrolytes capable of operating over wide temperature windows and delivering high safety, *Adv. Energy Mater.* 10 (2020) 2001235.
- [11] M.-T.F. Rodrigues, G. Babu, H. Gullapalli, K. Kalaga, F.N. Sayed, K. Kato, J. Joyner, P.M. Ajayan, A materials perspective on Li-ion batteries at extreme temperatures, *Nat. Energy* 2 (2017) 17108.
- [12] G. Zheng, S.W. Lee, Z. Liang, H.-W. Lee, K. Yan, H. Yao, H. Wang, W. Li, S. Chu, Y. Cui, Interconnected hollow carbon nanospheres for stable lithium metal anodes, *Nat. Nanotechnol.* 9 (2014) 618–623.
- [13] Z. Lu, J. Yu, J. Wu, M.B. Effat, S.C.T. Kwok, Y. Lyu, M.M.F. Yuen, F. Ciucci, Enabling room-temperature solid-state lithium–metal batteries with fluoroethylene carbonate-modified plastic crystal interlayers, *Energy Storage Mater.* 18 (2019) 311–319.
- [14] E. Cha, M.D. Patel, J. Park, J. Hwang, V. Prasad, K. Cho, W. Choi, 2d MoS₂ as an efficient protective layer for lithium metal anodes in high-performance Li–S batteries, *Nat. Nanotechnol.* 13 (2018) 337–344.
- [15] C. Sun, Y. Ruan, W. Zha, W. Li, M. Cai, Z. Wen, Recent advances in anodic interface engineering for solid-state lithium–metal batteries, *Mater. Horiz.* 7 (2020) 1667–1696.
- [16] W. Liu, P. Liu, D. Mitlin, Solid electrolyte interphases: review of emerging concepts in SEI analysis and artificial SEI membranes for lithium, sodium, and potassium metal battery anodes, *Adv. Energy Mater.* 10 (2020) 2070177.
- [17] A.L. Michan, B.S. Parimalam, M. Leskes, R.N. Kerber, T. Yoon, C.P. Grey, B.L. Lucht, Fluoroethylene carbonate and vinylene carbonate reduction: understanding lithium-ion battery electrolyte additives and solid electrolyte interphase formation, *Chem. Mater.* 28 (2016) 8149–8159.

- [18] S. Jiao, X. Ren, R. Cao, M.H. Engelhard, Y. Liu, D. Hu, D. Mei, J. Zheng, W. Zhao, Q. Li, N. Liu, B.D. Adams, C. Ma, J. Liu, J.-G. Zhang, W. Xu, Stable cycling of high-voltage lithium metal batteries in ether electrolytes, *Nat. Energy* 3 (2018) 739–746.
- [19] G. Cui, Reasonable design of high-energy-density solid-state lithium-metal batteries, *Matter* 2 (2020) 805–815.
- [20] Q. Wang, Z. Cui, Q. Zhou, X. Shangguan, X. Du, S. Dong, L. Qiao, S. Huang, X. Liu, K. Tang, X. Zhou, G. Cui, A supramolecular interaction strategy enabling high-performance all solid state electrolyte of lithium metal batteries, *Energy Storage Mater.* 25 (2020) 756–763.
- [21] P. López-Aranguren, M. Reynaud, P. Gluchowski, A. Bustinza, M. Galceran, J.M. López del Amo, M. Armand, M. Casas-Cabanas, Crystalline LiPON as a bulk-type solid electrolyte, *ACS Energy Lett.* 6 (2021) 445–450.
- [22] M. Balaish, J.C. Gonzalez-Rosillo, K.J. Kim, Y. Zhu, Z.D. Hood, J.L.M. Rupp, Processing thin but robust electrolytes for solid-state batteries, *Nat. Energy* (2021) n/a/n/a.
- [23] L. Long, S. Wang, M. Xiao, Y. Meng, Polymer electrolytes for lithium polymer batteries, *J. Mater. Chem. A* 4 (2016) 10038–10069.
- [24] J. Yu, Y.-Q. Lyu, J. Liu, M.B. Effat, S.C.T. Kwok, J. Wu, F. Ciucci, Enabling non-flammable Li-metal batteries via electrolyte functionalization and interface engineering, *J. Mater. Chem. A* 7 (2019) 17995–18002.
- [25] N. Boaretto, L. Meabe, M. Martínez-Ibáñez, M. Armand, H. Zhang, Review—Polymer electrolytes for rechargeable batteries: from nanocomposite to nanohybrid, *J. Electrochim. Soc.* 167 (2020) 070524.
- [26] S. Li, S.-Q. Zhang, L. Shen, Q. Liu, J.-B. Ma, W. Lv, Y.-B. He, Q.-H. Yang, Progress and perspective of ceramic/polymer composite solid electrolytes for lithium batteries, *Adv. Sci.* 7 (2020) 1903088.
- [27] D. Zhou, D. Shanmukaraj, A. Tkacheva, M. Armand, G. Wang, Polymer electrolytes for lithium-based batteries: advances and prospects, *Chem* 5 (2019) 2326–2352.
- [28] H. Wu, B. Tang, X. Du, J. Zhang, X. Yu, Y. Wang, J. Ma, Q. Zhou, J. Zhao, S. Dong, G. Xu, J. Zhang, H. Xu, G. Cui, L. Chen, LiDFOB initiated in situ polymerization of novel eutectic solution enables room-temperature solid lithium metal batteries, *Adv. Sci.* 7 (2020) 2003370.
- [29] X. Lin, J. Yu, M.B. Effat, Z. Guodong, M.J. Robson, S.C.T. Kwok, H. Li, S. Zhan, Y. Shang, F. Ciucci, Ultrathin and non-flammable dual-salt polymer electrolyte for high-energy-density lithium-metal battery, *Adv. Funct. Mater.* (2021) 2010261 n/a.
- [30] A.S. Westover, F.N. Shabat, J.W. Tian, S. Bernath, L. Oakes, W.R. Erwin, R. Carter, R. Bardhan, C.L. Pint, Stretching ion conducting polymer electrolytes: in-situ correlation of mechanical, ionic transport, and optical properties, *J. Electrochim. Soc.* 161 (2014) E112–E117.
- [31] Q. Zhao, S. Staln, C.-Z. Zhao, L.A. Archer, Designing solid-state electrolytes for safe, energy-dense batteries, *Nat. Rev. Mater.* 5 (2020) 229–252.
- [32] Y. Zheng, Y. Yao, J. Ou, M. Li, D. Luo, H. Dou, Z. Li, K. Amine, A. Yu, Z. Chen, A review of composite solid-state electrolytes for lithium batteries: fundamentals, key materials and advanced structures, *Chem. Soc. Rev.* 49 (2020) 8790–8839.
- [33] G. Xu, X. Shangguan, S. Dong, X. Zhou, G. Cui, Formulation of blended-lithium-salt electrolytes for lithium batteries, *Angew. Chem. Int. Ed.* 59 (2020) 3400–3415.
- [34] K. Xu, Nonaqueous liquid electrolytes for lithium-based rechargeable batteries, *Chem. Rev.* 104 (2004) 4303–4418.
- [35] R. Younesi, G.M. Veith, P. Johansson, K. Edström, T. Vegge, Lithium salts for advanced lithium batteries: Li–metal, Li–O₂, and Li–S, *Energy Environ. Sci.* 8 (2015) 1905–1922.
- [36] H. Yang, G.V. Zhuang, P.N. Ross, Thermal stability of LiPF₆ salt and Li-ion battery electrolytes containing LiPF₆, *J. Power Sources* 161 (2006) 573–579.
- [37] X. Wang, E. Yasukawa, S. Mori, Inhibition of anodic corrosion of aluminum cathode current collector on recharging in lithium imide electrolytes, *Electrochim. Acta* 45 (2000) 2677–2684.
- [38] K. Xu, S.S. Zhang, U. Lee, J.L. Allen, T.R. Jow, LiBOB: is it an alternative salt for lithium ion chemistry? *J. Power Sources* 146 (2005) 79–85.
- [39] C. Fu, Y. Ma, S. Lou, C. Cui, L. Xiang, W. Zhao, P. Zuo, J. Wang, Y. Gao, G. Yin, A dual-salt coupled fluoroethylene carbonate succinonitrile-based electrolyte enables Li–metal batteries, *J. Mater. Chem. A* 8 (2020) 2066–2073.
- [40] X. Chen, W. Xu, M.H. Engelhard, J. Zheng, Y. Zhang, F. Ding, J. Qian, J.-G. Zhang, Mixed salts of LiTFSI and LiBOB for stable LiFePO₄-based batteries at elevated temperatures, *J. Mater. Chem. A* 2 (2014) 2346–2352.
- [41] F. Li, Y. Gong, G. Jia, Q. Wang, Z. Peng, W. Fan, B. Bai, A novel dual-salts of LiTFSI and LiODFB in LiFePO₄-based batteries for suppressing aluminum corrosion and improving cycling stability, *J. Power Sources* 295 (2015) 47–54.
- [42] H. Xiang, P. Shi, P. Bhattacharya, X. Chen, D. Mei, M.E. Bowden, J. Zheng, J.-G. Zhang, W. Xu, Enhanced charging capability of lithium metal batteries based on lithium bis(trifluoromethanesulfonyl)imidate-lithium bis(oxalato)borate dual-salt electrolytes, *J. Power Sources* 318 (2016) 170–177.
- [43] X. Zhang, T. Liu, S. Zhang, X. Huang, B. Xu, Y. Lin, B. Xu, L. Li, C.-W. Nan, Y. Shen, Synergistic coupling between Li_{6.75}La₃Zr_{1.75}Ta_{0.25}O₁₂ and poly(vinylidene fluoride) induces high ionic conductivity, mechanical strength, and thermal stability of solid composite electrolytes, *J. Am. Chem. Soc.* 139 (2017) 13779–13785.
- [44] X. Zhang, S. Wang, C. Xue, C. Xin, Y. Lin, Y. Shen, L. Li, C.-W. Nan, Response to comment on “self-suppression of lithium dendrite in all-solid-state lithium metal batteries with poly(vinylidene difluoride)-based solid electrolytes, *Adv. Mater.* 32 (2020) 2000026.
- [45] J. Zheng, M.H. Engelhard, D. Mei, S. Jiao, B.J. Polzin, J.-G. Zhang, W. Xu, Electrolyte additive enabled fast charging and stable cycling lithium metal batteries, *Nat. Energy* 2 (2017) 17012.
- [46] V.D. Noto, S. Lavina, D. Longo, M. Vidali, A novel electrolytic complex based on δ -MgCl₂ and poly(ethylene glycol) 400, *Electrochim. Acta* 43 (1998) 1225–1237.
- [47] J. Hutter, M. Iannuzzi, F. Schiffrmann, J. VandeVondele, Cp2k: atomistic simulations of condensed matter systems, *Wiley Interdiscip. Rev. Comput. Mol. Sci.* 4 (2014) 15–25.
- [48] J. VandeVondele, M. Krack, F. Mohamed, M. Parrinello, T. Chassaing, J. Hutter, Quickstep: fast and accurate density functional calculations using a mixed gaussian and plane waves approach, *Comput. Phys. Commun.* 167 (2005) 103–128.
- [49] J. VandeVondele, J. Hutter, Gaussian basis sets for accurate calculations on molecular systems in gas and condensed phases, *J. Chem. Phys.* 127 (2007) 114105.
- [50] M. Krack, Pseudopotentials for H to Kr optimized for gradient-corrected exchange–correlation functionals, *Theor. Chem. Acc.* 114 (2005) 145–152.
- [51] J.P. Perdew, K. Burke, M. Ernzerhof, Generalized gradient approximation made simple, *Phys. Rev. Lett.* 77 (1996) 3865.
- [52] J. VandeVondele, J. Hutter, An efficient orbital transformation method for electronic structure calculations, *J. Chem. Phys.* 118 (2003) 4365–4369.
- [53] G. Bussi, D. Donadio, M. Parrinello, Canonical sampling through velocity rescaling, *J. Chem. Phys.* 126 (2007) 014101.
- [54] L. Martínez, R. Andrade, E.G. Birgin, J.M. Martínez, Packmol: a package for building initial configurations for molecular dynamics simulations, *J. Comput. Chem.* 30 (2009) 2157–2164.
- [55] G. Kresse, J. Furthmüller, Efficient iterative schemes for *ab initio* total-energy calculations using a plane-wave basis set, *Phys. Rev. B* 54 (1996) 11169.
- [56] G. Kresse, J. Furthmüller, Efficiency of *ab initio* total energy calculations for metals and semiconductors using a plane-wave basis set, *Comput. Mater. Sci.* 6 (1996) 15–50.
- [57] A.D. Becke, Density-functional thermochemistry. III. The role of exact exchange, *J. Chem. Phys.* 98 (1993) 5648–5652.
- [58] M.J. Frisch, G.W. Trucks, H.B. Schlegel, G.E. Scuseria, M.A. Robb, J.R. Cheeseman, G. Scalmani, V. Barone, B. Mennucci, G.A. Petersson, H. Nakatsuji, M. Caricato, X. Li, H.P. Hratchian, A.F. Izmaylov, J. Bloino, G. Zheng, J.L. Sonnenberg, M. Hada, M. Ehara, K. Toyota, R. Fukuda, J. Hasegawa, M. Ishida, T. Nakajima, Y. Honda, O. Kitao, H. Nakai, T. Vreven, J.A.J. Montgomery, J.E. Peralta, F. Ogliaro, M. Bearpark, J.J. Heyd, E. Brothers, K.N. Kudin, V.N. Staroverov, R. Kobayashi, J. Normand, K. Raghavachari, A. Rendell, J.C. Burant, S.S. Iyengar, J. Tomasi, M. Cossi, N. Rega, M.J. Millam, M. Klene, J.E. Knox, J.B. Cross, V. Bakken, C. Adamo, J. Jaramillo, R. Gomperts, R.E. Stratmann, O. Yazyev, A.J. Austin, R. Cammi, C. Pomelli, J.W. Ochterski, R.L. Martin, K. Morokuma, V.G. Zakrzewski, G.A. Voth, P. Salvador, J.J. Dannenberg, S. Dapprich, A.D. Daniels, Ö. Farkas, J.B. Foresman, J.V. Ortiz, J. Cioslowski, D.J. Fox, Gaussian 09, Revision D.01, Gaussian, Inc., Wallingford, CT, 2009.
- [59] P.E. Blöchl, Projector augmented-wave method, *Phys. Rev. B* 50 (1994) 17953.
- [60] M. Shakourian-Fard, G. Kamath, K. Smith, H. Xiong, S.K.R.S. Sankaranarayanan, Trends in Na-ion solvation with alkyl-carbonate electrolytes for sodium-ion batteries: insights from first-principles calculations, *J. Phys. Chem. C* 119 (2015) 22747–22759.
- [61] Q. Zhang, K. Wang, X. Wang, Y. Zhong, M. Liu, X. Liu, K. Xu, W. Fan, L. Yu, W. Li, Lithium bis(oxalate)borate reinforces the interphase on Li-metal anodes, *ACS Appl. Mater. Inter.* 11 (2019) 20854–20863.
- [62] S.S. Zhang, K. Xu, J.L. Allen, T.R. Jow, Effect of propylene carbonate on the low temperature performance of Li-ion cells, *J. Power Sources* 110 (2002) 216–221.
- [63] T. Hou, G. Yang, N.N. Rajput, J. Self, S.-W. Park, J. Nanda, K.A. Persson, The influence of FEC on the solvation structure and reduction reaction of LiPF₆/EC electrolytes and its implication for solid electrolyte interphase formation, *Nano Energy* 64 (2019) 103881.
- [64] S. Li, Y.-M. Chen, W. Liang, Y. Shao, K. Liu, Z. Nikolov, Y. Zhu, A superionic conductive, electrochemically stable dual-salt polymer electrolyte, *Joule* 2 (2018) 1838–1856.
- [65] D. Bresser, S. Lyonnard, C. Iojoiu, L. Picard, S. Passerini, Decoupling segmental relaxation and ionic conductivity for lithium-ion polymer electrolytes, *Mol. Syst. Des. Eng.* 4 (2019) 779–792.
- [66] R.C. Agrawal, G.P. Pandey, Solid polymer electrolytes: materials designing and all-solid-state battery applications: an overview, *J. Phys. D: Appl. Phys.* 41 (2008) 223001.
- [67] P. Martins, A.C. Lopes, S. Lanceros-Mendez, Electroactive phases of poly(vinylidene fluoride): determination, processing and applications, *Prog. Polym. Sci.* 39 (2014) 683–706.
- [68] L. Fan, S. Wei, S. Li, Q. Li, Y. Lu, Recent progress of the solid-state electrolytes for high-energy metal-based batteries, *Adv. Energy Mater.* 8 (2018) 1702657.
- [69] S.K. Karan, R. Bera, S. Paria, A.K. Das, S. Maiti, A. Maitra, B.B. Khatua, An approach to design highly durable piezoelectric nanogenerator based on self-poled PVDF/AIO-rGO flexible nanocomposite with high power density and energy conversion efficiency, *Adv. Energy Mater.* 6 (2016) 1601016.
- [70] X. Cai, T. Lei, D. Sun, L. Lin, A critical analysis of the α , β and γ phases in poly(vinylidene fluoride) using FTIR, *RSC Adv.* 7 (2017) 15382–15389.
- [71] Y. Bormashenko, R. Pogreb, O. Stanevsky, E. Bormashenko, Vibrational spectrum of PVDF and its interpretation, *Polym. Test.* 23 (2004) 791–796.
- [72] K.M. Diederichsen, E.J. McShane, B.D. McCloskey, Promising routes to a high Li⁺ transference number electrolyte for lithium ion batteries, *ACS Energy Lett.* 2 (2017) 2563–2575.
- [73] G.B. Appetecchi, F. Croce, B. Scrosati, Kinetics and stability of the lithium electrode in poly(methylmethacrylate)-based gel electrolytes, *Electrochim. Acta* 40 (1995) 991–997.
- [74] S.K. Heiskanen, J. Kim, B.L. Lucht, Generation and evolution of the solid electrolyte interphase of lithium-ion batteries, *Joule* 3 (2019) 2322–2333.
- [75] S.H.-S. Cheng, C. Liu, F. Zhu, L. Zhao, R. Fan, C.-Y. Chung, J. Tang, X. Zeng, Y.-B. He, (oxalato)borate: the key ingredient for polyethylene oxide based composite electrolyte to achieve ultra-stable performance of high voltage solid-state LiNi_{0.8}Co_{0.1}Mn_{0.1}O₂/lithium metal battery, *Nano Energy* 80 (2021) 105562.